Inorganic Chemistry

Article

pubs.acs.org/IC

A Synthetically Generated $LFe^{IV}OH_n$ Complex

Andrew C. Weitz, Matthew R. Mills, Alexander D. Ryabov, Terrence J. Collins, Yisong Guo, Emile L. Bominaar,* and Michael P. Hendrich*

Department of Chemistry, Carnegie Mellon University, 4400 Fifth Avenue, Pittsburgh, Pennsylvania 15213, United States

Supporting Information

ABSTRACT: High-valent Fe−OH species are important intermediates in hydroxylation chemistry. Such complexes have been implicated in mechanisms of oxygen-activating enzymes and have thus far been observed in Compound II of sulfur-ligated heme enzymes like cytochrome P450. Attempts to synthetically model such species have thus far seen relatively little success. Here, the first synthetic $Fe^{IV}OH_n$ complex has been generated and spectroscopically characterized as either $[LFe^{IV}OH]^-$ or $[LFe^{IV}OH_2]^0$, where $H_4L = Me_4C_2(NHCOCMe_2NHCO)_2CMe_2$ is a variant of a tetra-amido macrocyclic ligand (TAML). The steric bulk provided by the replacement of the aryl group with the $-CMe_2CMe_2-$ unit in this TAML variant prevents dimerization in all oxidation states over a wide pH range, thus allowing the generation of $Fe^{IV}OH_n$ in near quantitative yield from oxidation of the $[LFe^{III}OH_2]^-$ precursor.

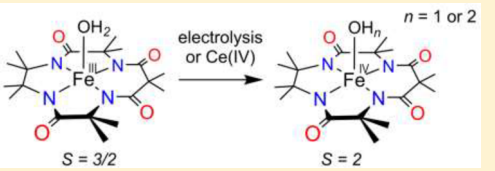

INTRODUCTION

Cytochrome P450 enzymes activate dioxygen to functionalize a broad range of biologically active molecules.[1] After dioxygen activation, cytochrome P450 generates a Compound I state composed of an $Fe^{IV}O$ with a porphyrin radical cation, two oxidizing equivalents above the resting Fe^{III} state. Compound I then abstracts a hydrogen atom from the substrate to form an $Fe^{IV}OH$ species (Compound II) and substrate radical, which rapidly forms a hydroxylated product and Fe^{III}. The efficiency of the enzyme in this process has been tied to the stability of the protonated Compound II intermediate, which in turn is assisted by an electron-rich thiolate residue ligated axially to the heme. Hydrogen bonding to nearby residues may also stabilize the protonated Compound II intermediate and prevent unproductive oxidation of nearby tyrosine residues.[2−4] Green et al. suggest the axial thiolate lowers the reduction potential of the iron and increases the pK_a of $Fe^{IV}O$ to ∼12, thereby preventing oxidation of nearby Tyr and Trp residues.[4]

Attempts to synthetically model $Fe^{IV}OH$ species have been thus far not successful. Hill et al. describes work on a protonated $Fe^{IV}O$ complex with H-bonding interactions to support the oxo unit, but protonation was found to occur on the ligand rather than the iron−oxo unit.[5] Zaragoza et al. report an iron corrole complex one redox level above $Fe^{III}OH$ but caution that it could be an $Fe^{III}(corrole^{+\bullet})$ complex.[6] Here, we present evidence that a stable synthetically generated $LFe^{IV}OH/LFe^{IV}OH_2$ species is produced from a recently developed Fe^{III} variant of TAML activator **1** that represents a "beheaded" version of prototype TAML macrocycle **2**, in which the benzene ring is replaced with the tetramethylated ethyl unit (Figure 1).[7] Complex **1** was shown to have the highest pK_a (11.4) of all Fe^{III} TAML variants ($[\mathbf{1}\text{-}Fe^{III}(OH_2)]^- \rightleftarrows [\mathbf{1}\text{-}Fe^{III}(OH)]^{2-} + H^+$), and the $Fe^{V}O$ state of **1** was observed to be remarkably stable in water at room temperature in a wide pH range.[7,8] Furthermore, the substitution of the planar aryl ring with the out of plane methyl groups increased steric interaction to discourage $Fe^{IV}(\mu\text{-oxo})$ dimer formation, as dimer formation occurs for other TAML compounds.[9] The lack of aromatic rings in **1** also stabilizes higher iron oxidations state rather than ring oxidation, as has been previously observed for some TAML variants.[10,11] The decreased acidity of the Fe^{III} center of **1** suggested the possibility of stabilizing an $Fe^{IV}OH$ species. Replacement of the aryl group with the $-CMe_2CMe_2-$ unit, in addition to the strong electron donating amide donors of TAML, could provide an overall electron donation to the iron of the 5-coordinate complex that is comparable to that of 6-coordinate P450-type iron sites with an axial thiolate ligand.

As reported previously, the coordination environment of iron in **1** varies as a function of pH, with $[\mathbf{1}\text{-}Fe^{III}(OH_2)]^-$ dominating below pH 11.4 and $[\mathbf{1}\text{-}Fe^{III}(OH)]^{2-}$ at pH > 11.4.[7] Previous results indicated that **1** reacted with NaClO via two distinct, pH-dependent oxidation pathways: Fe^{III} reacts with NaClO with a 1:1 stoichiometry at pH below 10.5 to immediately generate $Fe^{V}O$, while above pH 10.5, the stoichiometry is 2:1 (Fe^{III}/NaClO) to generate the monomeric $Fe^{IV}O$ species. The formation of a stable $Fe^{V}O$ species at room temperature in water at such a wide pH range was unprecedented.[8] The stability of these high-valent species offered greater accessibility for studies of their spectroscopic properties. The absence of $Fe^{IV}(\mu\text{-oxo})$ dimers as oxidation products was attributed to the steric hindrance from the four out-of-plane methyl groups. Furthermore, given the enhanced stability of the both high-valent species and the increased pK_a of the axial water ligand of $[\mathbf{1}\text{-}Fe^{III}(OH_2)]^-$ relative to that of other TAMLs, it was conceivable that the pK_a of the oxo unit of the $Fe^{IV}O$ state is also higher. Upon Fe^{III} oxidation in water

Received: November 15, 2018

DOI: 10.1021/acs.inorgchem.8b03200
Inorg. Chem. XXXX, XXX, XXX−XXX

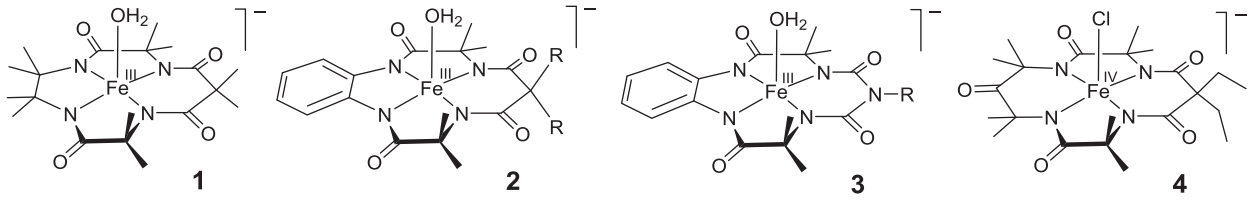

Figure 1. TAML activators used or mentioned in this work.

Table 1. Electronic and Nuclear Parameters of Selected TAML Complexes[a]

complex	spin	δ (mm/s)	ΔE_Q (mm/s)	D (cm^{-1})	E/D	A (T)[a]	η	ref
[**1**-Fe^{V}O]$^{1-}$	1/2	−0.48	+4.7			−48, +1, 0	0.7	8
		−0.48	*+4.85*			*−40, −6, −1*	0.8	
[**1**-Fe^{IV}O]$^{2-}$	1	−0.20	+4.11	+25(2)	~0	−27, −29, −3	0.03	*b*
		−0.18	*+3.53*	*+10*		*−26, −25, −5*	*0.07*	
green exp.	2	−0.12	+0.65	−3.5(5)	0.14	−14, −18, −9[c]	0.7	
[**1**-Fe^{IV}OH]$^{-}$	2	*−0.12*	*−1.01*	*−1.5*	*0.06*	*−16, −16, −9*	0.4	*b*
[**1**-Fe^{IV}OH$_2$]^{0}	2	*−0.13*	*+1.37*	*−1.8*	*0.02*	*−16, −15, −10*	*0.6*	
[**2**-Fe^{IV}O]$^{2-}$	1	−0.19	+3.95	24(3)	~0	−27, −27, +2	0	26
		−0.17	*+3.35*			*−24, −24, −4*	*0*	
[**4**-Fe^{IV}Cl]$^{-}$	2	−0.04	−0.89	−2.6	0.14	−18, −15, −11	0.2	31
		−0.06	*−0.99*	*−1.1*	*0.08*	*−17, −16, −11*	*0.4*	

[a]DFT-calculated parameters are in *italic*. DFT values obtained by adding the experimental value for the isotropic value of **A** to the **A**(spin-dipolar) from DFT. [b]This work. [c]Both *A*- and EFG-tensors are rotated about *y*-axis by 20°.

in absence of Cl$^-$, all known TAMLs are observed as either Fe^{IV}O or Fe^{IV}(μ-oxo) dimers, suggesting that either the pK_a of the oxo unit is low or the protonated form is unstable and leads to the dimer formation. Here we explored the possibility of generating a protonated Fe^{IV}O species at low pH and were able to successfully observe a low pH Fe^{IV} species with markedly unique spectroscopic properties distinguishing it from all known Fe^{IV}O TAML compounds. We use spectroscopic and DFT methods to demonstrate the generation of the first synthetic Fe^{IV}OH or Fe^{IV}OH$_2$ species.

METHODS

1 Preparation and ^{57}Fe Enrichment. **1** was prepared as previously described.[7] ^{57}Fe-enriched **1** was prepared by metalation with ^{57}Fe-enriched $FeCl_3$. $^{57}FeCl_3$ was synthesized by bubbling HCl gas through a suspension of ^{57}Fe powder in ethanol. After 2 h the solvent was removed by rotary evaporation. The remaining solid was put under high vacuum overnight and used without further purification. The solid was purified by column chromatography on basic alumina using CH_2Cl_2/MeOH/NEt_3 (90%/5%/5%) as described previously.[12]

Electrochemistry and Spectroelectrochemistry of 1. Electrochemical studies were performed with an Autolab PGSTAT100. The working electrode was a glassy carbon disk, with a saturated calomel reference electrode and platinum wire counter electrode. For bulk electrolysis, the working electrode was a platinum coil. Samples were brought to the appropriate potential, and then quickly transferred to cuvette, EPR, tube, or Mössbauer cup for analysis by electronic absorption, EPR, or Mössbauer spectroscopy, respectively. For chemically oxidized samples, one equivalent of a fresh cerium(IV) ammonium nitrate solution in 0.1 M $HClO_4$ was added to produce the Fe^{4+} complex.

EPR and Mössbauer Spectroscopies. X-band EPR spectra were recorded on a Bruker ELEXSYS spectrometer equipped with an Oxford ESR-910 liquid helium cryostat and a Bruker bimodal cavity for generation of microwave fields parallel and transverse to the applied magnetic field. The quantification of all signals was measured relative to a CuEDTA spin standard prepared from a copper atomic absorption standard (Sigma-Aldrich). The microwave frequency was calibrated with a frequency counter, and the magnetic field was measured with a NMR gaussmeter. The sample temperature was calibrated against a calibrated cernox sensor (Lakeshore CX-1050) mounted inside an EPR tube. A modulation frequency of 100 kHz was used for all EPR spectra. Mössbauer spectra were recorded on either a variable field or a weak-field spectrometer operating in a constant acceleration mode in a transmission geometry using Janis Research Inc. cryostats that allow for a variation in temperature from 4 to 300 K. One of the dewars housed a superconducting magnet that allowed for the application of magnetic fields up to 8 T parallel to the γ-radiation. Isomer shifts are reported relative to Fe metal at 298 K. The simulation software *SpinCount* was written by one of the authors.[13] The software diagonalizes the electronic terms of the spin Hamiltonian:

$$H = \beta \mathbf{S}\cdot\mathbf{g}\cdot\mathbf{B} + \mathbf{S}\cdot\mathbf{D}\cdot\mathbf{S} + \mathbf{S}\cdot\mathbf{A}\cdot\mathbf{I} - g_n\beta_n\mathbf{B}\cdot\mathbf{I} + \mathbf{I}\cdot\mathbf{P}\cdot\mathbf{I}$$

$$\mathbf{S}\cdot\mathbf{D}\cdot\mathbf{S} = D[S_z^2 - S(S+1)/3 + (E/D)(S_x^2 - S_y^2)]$$

$$\mathbf{I}\cdot\mathbf{P}\cdot\mathbf{I} = (eQV_{zz}/12)[3I_z^2 - I(I+1) + \eta(I_x^2 - I_y^2)]$$

where the parameters have the usual definitions,[14] and performs least-squares fitting of simulations to the spectra. The quantitative simulations are generated with consideration of all intensity factors, which allows computation of simulated spectra for a specified sample concentration.

NRVS Methods. The ^{57}Fe nuclear resonance vibrational spectroscopy (NRVS) data were recorded using published procedures on multiple occasions at beamline 3-ID at the Advanced Photon Source (APS).[15,16] The incident flux provided by the beamline is ~2 × 10^9 photons/s in a 1 meV bandwidth centered at 14.4125 keV in a 1 mm (vertical) x 3 mm (horizontal) spot. The monochromators used in the experiment consisted of a water-cooled diamond (1,1,1) double crystal with 1.1 eV bandpass, followed by two separate Si(4,0,0) and Si(10,6,4) channel-cut crystals in a symmetric geometry. During the measurements, samples were maintained at low temperatures using a closed-cycle helium cryostat. The temperature for individual spectra were calculated using the ratio of anti-Stokes to Stokes intensity according to $S(-E) = S(E)\exp(-E/kT)$ and were generally in the

DOI: 10.1021/acs.inorgchem.8b03200
Inorg. Chem. XXXX, XXX, XXX−XXX

range of 40−80 K. Spectra were recorded between −40 and 120 meV in 0.25 meV steps. Delayed nuclear fluorescence and iron K fluorescence (from internal conversion) were recorded with a single avalanche photodiode detector (APD) with 1 cm^2 detection area. Each scan required about 50 min, and all scans were added and normalized to the intensity of the incident beam. The ^{57}Fe partial vibrational density of state (PVDOS) was extracted from the raw NRVS data using the PHOENIX software package.[17]

DFT Methodology. The isomer shift (δ), quadrupole splitting (ΔE_Q), and spin-dipolar contribution to the A values in Tables 1 and S1 were obtained for optimized geometries, using the hybrid functional B3LYP and basis set 6-311G provided by $G'09$.[18] ΔE_Q was converted from atomic units to mm/s using the conversion factor −1.6 mm s^{-1}/AU; the δ calculations used a TAML adapted version of calibrations,[19] obtained by adding −0.05 mm/s to the δ values from the original calibration. The calculation for the NRVS vibrational energies used BP86/TZVP optimized geometries and frequencies to which no scaling factor was applied. The DFT values for the zero-field splitting parameter D listed in Table 1 were obtained for the $G'09$ B3LYP/6-311G optimized structures with the program suite ORCA developed by Neese and co-workers,[20] using functional B3LYP and basis set def2-TZVP(-f).[21,22] The frequency analysis for Figure 5 was performed with BP86/TZVP using $G'09$. The NRVS spectra were generated by using the DFT normal mode energies as line positions and the ^{57}Fe displacements for evaluating the line intensity factors.[23]

RESULTS

Electrochemical Evidence for a Fe^{IV} Species. The [**1**-$Fe^{V}O$]$^-$ species is cleanly produced when **1** is oxidized by the two-electron oxidant NaClO at pH 2.[8,24] No indications for the intermediacy of an Fe^{IV} species were revealed when the reaction was followed by electronic absorption spectroscopy consistent with the concerted 2e$^-$ oxygen transfer mechanism of reaction 1.

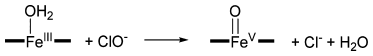

(1)

In contrast, cyclic voltammetry (CV) and differential pulse voltammetry (DPV) scans applied to **1** at pH 2 gave evidence for an intermediate species. There were two reversible features in the CV of **1** in the range of 0.0−1.5 V vs SCE (Figure 2A). The waves at 0.89 and 1.25 V are consistent with $Fe^{III/IV}$ and $Fe^{IV/V}$ transitions, respectively. The DPV of **1** (Figure 2A) provides further evidence for two species and shows current amplitudes of equal intensity, and hence a similar number of electrons are moved (one) within each. Cyclic voltammograms (CVs) up to 1.1 V vs SCE as a function of pH are shown in Figure S2. Between pH 3 and 10.5, the CV ceased to exhibit reversible characteristics suggesting an unstable species (Figure S2). However, at pH 2.0, 2.5, and 3.0, the CVs are very similar to the peak separation of approximately 60 mV, indicating that the protonation state of the complex does not change for the $Fe^{III/IV}$ transition.

Although all TAMLs of previous generations provided noninformatively broad and poorly reproducible CVs in water,[25] **1** was an opposite case revealing Nernstian one-electron CVs at pH 2 for $Fe^{III/IV}$ and $Fe^{IV/V}$. The peak separation of 58 mV, was near the ideal limit of 59 mV for reversible one-electron transfer. Furthermore, identical anodic and cathodic currents ($i_a = i_c$) and linearity of i_a or i_c against $v^{1/2}$ (square root of the scan rate) were observed for v in the ranges of 10−150 mV s^{-1} and 0−1 V (Figure S1).

The CVs of **1** changed significantly upon increasing the pH to 13.0 (Figure 2B). As at pH 2.0, the $Fe^{III/IV}$ and $Fe^{IV/V}$ transitions were reversible and peak currents were similar. At pH 13.0, the axial ligand of **1** was shown previously to change

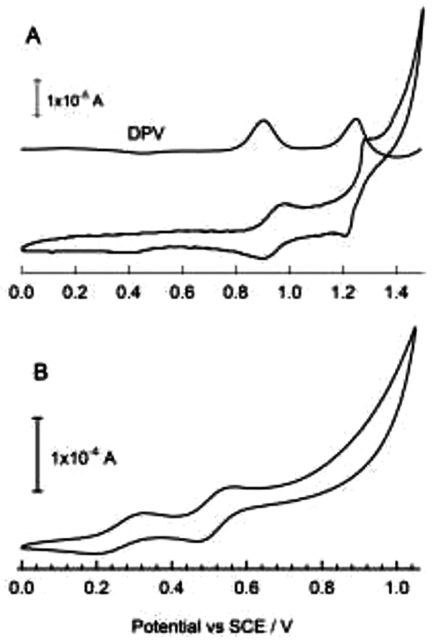

Figure 2. CV and differential pulse voltammograms (DPV) of **1** (1×10^{-3} M) at (A) pH 2 and (B) pH 13. Conditions: aqueous buffer (0.1 M phosphate/citrate/borate) at 25 °C, glassy carbon electrode, scan rate 0.1 V/s.

from [**1**-$Fe^{III}(OH_2)$]$^{1-}$ to [**1**-$Fe^{III}(OH)$]$^{2-}$ with pK_a = 11.4.[7] Thus, we expect the ground states for the CV of Figure 2 to differ by a proton. At pH 13.0, the final states for Fe^{IV} and Fe^{V} species were [**1**-$Fe^{IV}O$]$^{2-}$ and [**1**-$Fe^{V}O$]$^-$, respectively, as shown below. Therefore, it was expected that $E_{1/2}$ for the $Fe^{IV/V}$ transition was pH-independent, while $E_{1/2}$ for the $Fe^{III/IV}$ transition shifted to a more negative potential as the pH increased in the range of 10.5−13.5 with a slope of 50 mV/pH (Figure S2), close to the Nernstian value of 59 mV/pH anticipated for a $1H^+/1e^-$ coupled electron transfer.

DPV data were previously reported for **2** obtained under basic conditions (pH 12.6) when the $Fe_2^{IV}(\mu$-O) dimer is not formed and [**2**-$Fe^{IV}O$]$^{2-}$ is the only species present.[9] Two peaks were observed at 0.66 and 0.88 V vs SCE. The waves were assigned to the $Fe^{III/IV}$ and $Fe^{IV/V}$ transitions, respectively. The results of this work support those assignments. The elimination of the $Fe_2^{IV}(\mu$-O) dimer was achieved in **2** by increasing pH, and in **1** by introducing steric bulk.

Based on the above electrochemical results, we performed bulk electrolysis at both pH 2 and pH 13 to generate iron species for spectroscopic characterizations. Application of a constant potential of 1.2 V vs SCE at pH 2, just below the onset of the second event, generated an electronic absorption spectrum of a new green species (Figure 3A) with λ_{max} = 620 nm (ε = 5100 M^{-1} cm^{-1}). The spectrum of this green species was reproduced by one electron oxidation of **1** with $(NH_4)_2[Ce(NO_3)_6]$ (Figure S3); therefore, the spectrum of Figure 3A corresponds to an Fe^{IV} species. Application of a constant potential of 1.5 V vs SCE at pH 2 generated a species with λ_{max} = 450 nm in 72% yield with an electronic absorption spectrum (Figure 3B) identical to that of [**1**-$Fe^{V}O$]$^-$ generated with NaClO.[8] The [**1**-$Fe^{V}O$]$^-$ species converted to the new green species (λ_{max} = 620) with a pseudo-first-order rate constant k_{obs} of 0.013 ± 0.03 s^{-1} at 13 °C. In turn, the green species decayed further to afford a mixture of **1** together with products of its degradation with k_{obs} of (3.1 ± 0.2) × 10^{-3} s^{-1}.

DOI: 10.1021/acs.inorgchem.8b03200
Inorg. Chem. XXXX, XXX, XXX−XXX

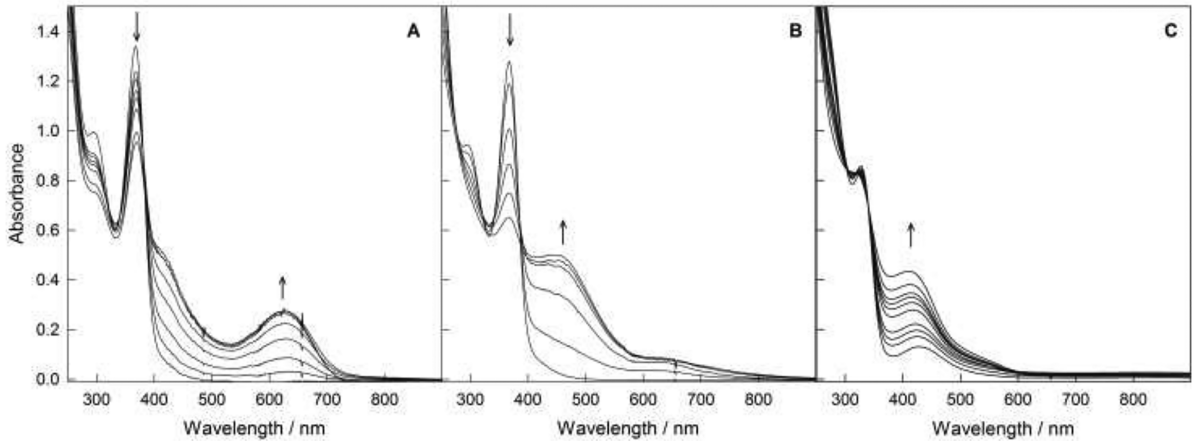

Figure 3. Spectra generated by bulk electrolysis of 1 mM **1** at 1.2 V, pH 2 (A); 1.5 V, pH 2 (B); and pH 13 (C). Conditions: 0.1 M $NaClO_4$ at 0 °C. Spectra A and B are recorded every 5 and 10 min, respectively. The first three spectra from bottom in C were obtained after 10, 20, and 40 min at electrode potential of 0.75 V. The next three spectra were generated at 10 min intervals after increasing the voltage to 0.85 V. The final two spectra are at 10 min intervals after increasing the voltage to 1.2 V.

The effect of raising pH on the green species was not examined owing to the short lifetime of the species.

At pH 13, only the $[\mathbf{1}\text{-}Fe^{IV}O]^{2-}$ species (λ_{max} = 410 nm) could be generated via bulk electrolysis at 1.2 V in 73% yield (Figure 3C). No spectroscopic features of the $[\mathbf{1}\text{-}Fe^{V}O]^{-}$ species were observed despite the evidence from CV for its existence. This agrees with previous results that demonstrated oxidation of **1** by NaClO at pH 13 formed only $[\mathbf{1}\text{-}Fe^{IV}O]^{2-}$; thus, $[\mathbf{1}\text{-}Fe^{V}O]^{-}$ at this pH was not stable.[8] When the $[\mathbf{1}\text{-}Fe^{IV}O]^{2-}$ species was acidified to pH 2 with concentrated phosphoric acid, the compound underwent rapid disproportionation to afford equal quantities of $[\mathbf{1}\text{-}Fe^{III}(OH)]^{2-}$ and $[\mathbf{1}\text{-}Fe^{V}O]^{-}$ derivatives as shown by UV−vis spectroscopy.

Spectroscopy of S = 1 $[\mathbf{1}\text{-}Fe^{IV}O]^{2-}$ Species. In our effort to determine the properties of the new green species (λ_{max} = 620 nm), we first present results for $[\mathbf{1}\text{-}Fe^{IV}O]^{2-}$ (λ_{max} = 410 nm) and $[\mathbf{1}\text{-}Fe^{V}O]^{1-}$ (λ_{max} = 450 nm). The latter two species have been partially characterized previously[8] and are similar to other previously well characterized TAML complexes.[26−28] The additional characterization presented here highlights the significant departure of electronic properties of the new green species (λ_{max} = 620 nm) from other TAML species.

An ^{57}Fe-enriched sample of **1** was oxidized by 1 equiv of NaClO at pH 13 to form $[\mathbf{1}\text{-}Fe^{IV}O]^{2-}$ with λ_{max} = 410 nm. Prior to oxidation, the EPR and Mössbauer spectra reproduced the published spectra of **1**.[8] After oxidation, the EPR spectrum of a corresponding sample showed loss of the Fe^{III} species, with no new signals appearing. Figure 4 shows Mössbauer spectra of the oxidized species recorded with variable temperatures and fields. In low field, the oxidized species has parameters of δ = −0.20 mm/s and ΔE_Q = +4.11 mm/s which are in agreement with a previous report.[8] Here, the magnetic field dependence of the species are presented, from which are derived additional electronic and hyperfine parameters. The sample showed 85% conversion to Fe^{IV} with 15% of unreacted **1** which was best observed in Figure 4C from the peaks near 0 and 4 mm/s marked by arrows. For S = 1 iron centers with a large zero-field parameter (D > 20 cm^{-1}), the m_s = ± 1 states populate measurably at temperatures above 25 K, making the spectra sensitive to the A-tensor and D-value. These values were determined from the simulations as shown in Figure 4 and listed in Table 1. The values for D, δ, ΔE_Q and the A-tensor are

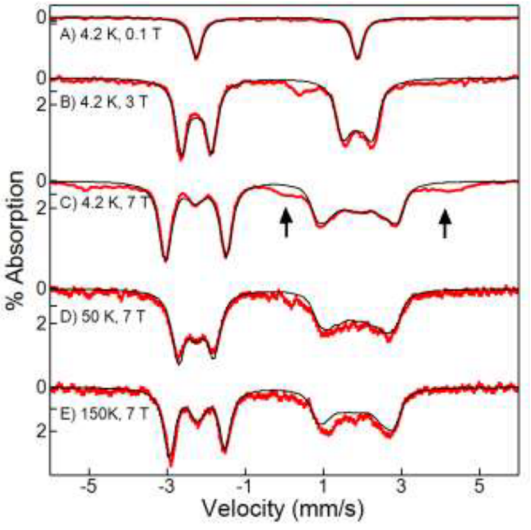

Figure 4. Mössbauer spectra of $[\mathbf{1}\text{-}Fe^{IV}O]^{2-}$ prepared from oxidation of **1** at pH 13 oxidized with 1 equiv of NaClO. The spectra were recorded at the applied fields and sample temperatures listed in the figure. The black traces are simulations using the parameters given in Table 1 for S = 1.

all close to those of previously characterized monomeric S = 1 $Fe^{IV}O$ complexes of TAML.[9,26]

NRVS were recorded on the ^{57}Fe-enriched Mössbauer sample of $[\mathbf{1}\text{-}Fe^{IV}O]^{2-}$ generated at pH 13 used for the spectra of Figure 4. The NRVS-derived ^{57}Fe partial vibrational density of state (PVDOS) spectrum at 40 K is shown in Figure 5B. The spectrum exhibits a peak at 763 cm^{-1} which was attributed to an Fe^{IV}−O vibration. This value is at the lower end of the range of characterized nonheme Fe^{IV}−O vibration energies and is comparable to the Fe^{IV}−O vibration at 798 cm^{-1} for the species generated from oxidation of **3**.[29,30] The spectral features below 600 cm^{-1} can be attributed to Fe−N vibrations from the TAML ligand.

Spectroscopy of S = 1/2 $[\mathbf{1}\text{-}Fe^{V}O]^{1-}$ Species. ^{57}Fe-enriched samples of **1** were oxidized with 3 equiv of NaClO at pH 1 and 7. Previously, the resulting oxidized species was found to be stable at room temperature in water in the pH range of 1−10.5, and characterized by electronic absorption,

DOI: 10.1021/acs.inorgchem.8b03200
Inorg. Chem. XXXX, XXX, XXX−XXX

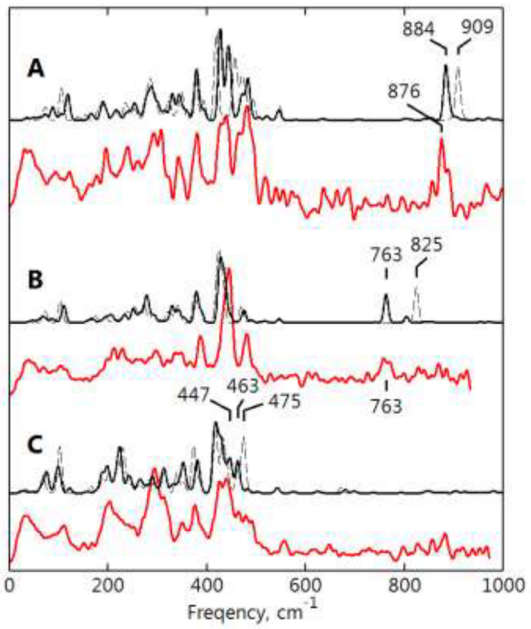

Figure 5. NRVS of oxidized complexes (red traces): (A) [**1**-Fe^{V}O]$^{-}$, pH 13, (B) [**1**-Fe^{IV}O]$^{2-}$, pH 13, and (C) 620 nm green species. The black traces are simulations from DFT frequency calculations with (solid) and without (dashed) hydrogen bonding to solvent water molecule(s); one water for A and C, and two waters for B.

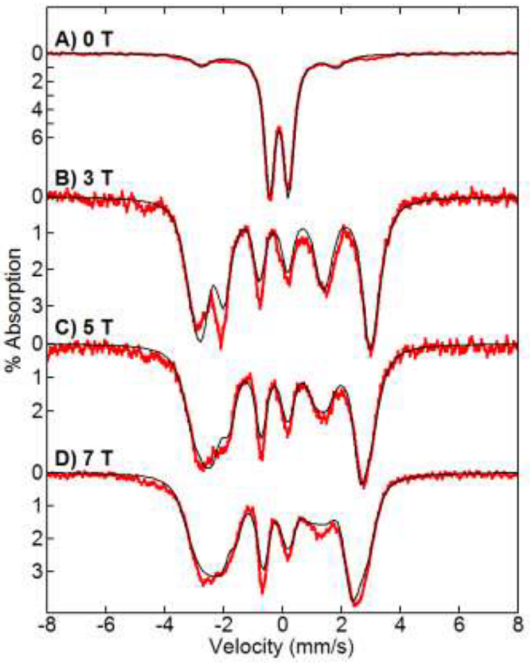

Figure 6. Mössbauer spectra of 620 nm green species recorded at 4.2 K for magnetic fields listed. The simulations (black traces) are calculated for $S = 2$ with the parameters listed in Table 1. The outer features in A at ca. −2.5, 2 mm/s are from a minor amount of [**1**-Fe^{V}O]$^{-}$.

EPR, and Mössbauer spectroscopies to be [**1**-Fe^{V}O]$^{1-}$.[8] Mössbauer spectra of the pH 1 and 7 samples confirmed generation of the same [**1**-Fe^{V}O]$^{1-}$ species in 78% yield. The NRVS-derived ^{57}Fe PVDOS spectrum of [**1**-Fe^{V}O]$^{1-}$ showed an intense peak at 876 cm^{-1} which was attributed to the Fe^{V}−O vibration (Figure 5A). The high value is consistent with a shorter bond length expected for Fe^{V}−O relative to Fe^{IV}−O and is comparable to the previously reported Fe^{V}−O vibration at 862 cm^{-1} for the species generated from oxidation of **3**.[30] In addition, the ^{57}Fe PVDOS spectrum was identical for samples prepared at pH 1 and 7.

Spectroscopy of Green Fe^{IV} Species. As described above, the electrochemical data indicated the presence of a Fe$^{III/IV}$ couple at a potential of +0.89 V for pH 2. Both bulk electrolysis at +1.2 V, pH 2 of **1** and oxidation of **1** with 1.1 equiv of Ce^{IV} at pH 1 and 2 generated a stable new green species with λ_{max} = 620 nm (Figure 3A). Mössbauer, EPR, and NRVS samples of the green species were prepared similarly by oxidation of **1** with Ce^{IV} at pH 1. The Mössbauer spectra recorded at a temperature of 4 K are shown in Figure 6. The spectrum in zero magnetic field was composed of two species. The major species (87% of total iron) had parameters of δ = −0.12 mm/s and ΔE_Q = +0.65 mm/s (Table 1). The minor species (13% of total iron) showed a doublet with parameters of δ = −0.48 mm/s and ΔE_Q = 4.7 mm/s. The EPR spectra will be discussed below and required a high-spin $S = 2$ iron center for the major species. The Mössbauer simulations of the majority species shown in Figure 6 are for $S = 2$ and determined the parameters given in Table 1. The parameters of the minority species matched those for [**1**-Fe^{V}O]$^{-}$ at pH 1, and its presence is consistent with a slight excess of Ce^{IV} used in oxidation of 1.[8] The high concentration and low pH of the sample likely contributed to some aggregation and increased electronic relaxation rates to generate a doublet, rather than a magnetic pattern for the $S = 1/2$ [**1**-Fe^{V}O]$^{-}$ species.

An EPR spectrum of the green species is shown in Figure 7. In perpendicular mode, the $S = 3/2$ EPR signal of **1** vanished. In parallel mode, a new resonance was observed near g = 11. This same signals as observed by EPR and Mössbauer spectroscopies were also observed from samples containing

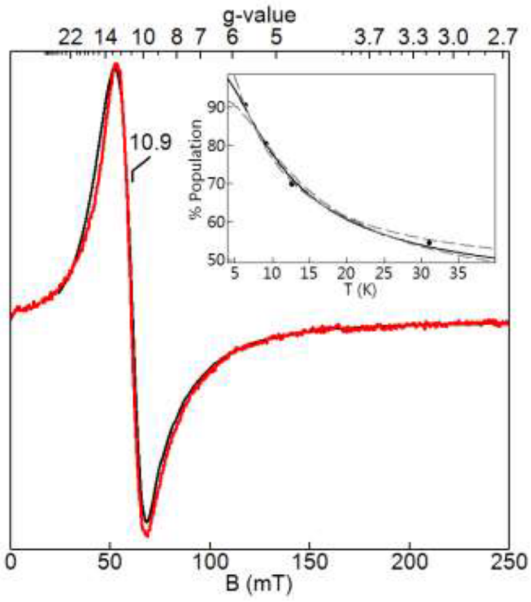

Figure 7. Parallel mode EPR spectra (red, 9.331 GHz, 0.2 mW, 6 K) and simulation (black) of the 620 nm green species. Simulation parameters: $S = 2$, $D = -3.5$ cm^{-1}, $E/D = 0.14$, $g_z = 2.2$. Inset: Signal intensity times temperature versus temperature (•) fitted to the % population of the ground doublet of the $S = 2$ multiplet for D = −3.5(5) cm^{-1} (dashed lines are ±1 cm^{-1}).

DOI: 10.1021/acs.inorgchem.8b03200
Inorg. Chem. XXXX, XXX, XXX−XXX

the green species that were produced from bulk electrolysis of **1** as described above. Thus, the spectroscopy of the green species described here is independent of the two methods of oxidation. The EPR signal intensity was measured as a function of temperature and is shown in the inset of Figure 7. The spectrum and temperature dependence of Figure 7 were simulated using eq 1 for $S = 2$, and the results are overlaid on the data for the parameters given in the caption. The simulations allow measurement of the species concentration, which gave a concentration in agreement with the iron concentration of the sample and unambiguously identify the green species as an $S = 2$ species. The parameters are in agreement with those determined from the Mössbauer spectra. Thus, the EPR and Mössbauer data indicate that the new green species is high-spin $S = 2$ Fe^{IV}.

The high-spin configuration of the new green species is rare when compared to previously characterized Fe^{IV} complexes of TAML. The only other known Fe^{IV} TAML high-spin $S = 2$ complex is $[\mathbf{4}\text{-}Fe^{IV}Cl]^-$ (Figure 1).[31] The Mössbauer parameters of the green species are also comparable to those of $[\mathbf{4}\text{-}Fe^{IV}Cl]^-$ (Table 1).[31] As for $[\mathbf{4}\text{-}Fe^{IV}Cl]^-$, the isotropic value of the A-tensor is −14 T; a value which is considerably lower than the expected free ion Fe^{4+} value of approximately −35 T. The significantly more positive value is attributed to metal bond covalency of TAML. To demonstrate that the new green species is unrelated to the chloride complex, samples were passed through an anion exchange column to remove any residual Cl^- ions from the starting material. After treatment with 1 equiv of Ce^{4+}, the resulting green species gave the same EPR signal as that in Figure 7. Furthermore, samples prepared in the presence of 1 M Cl^- and oxidation with 1 equiv of Ce^{4+} showed a new parallel mode EPR signal from an $S = 2$ species at $g = 14.7$ with different zero-field parameters than those of the green species (Figure S4), indicating substitution of the axial ligand for chloride. This is consistent with the low affinity of TAML variants for Cl^- in an aqueous environment ($K_D(Cl^-) > 0.5$ M).[32]

NRVS-derived ^{57}Fe PVDOS spectra of the green species, from the same Mössbauer sample used in the spectra of Figure 6, are shown in Figure 5C. The $Fe^V{=}O$ and $Fe^{IV}{=}O$ vibrations at 876 and 763 cm^{-1} observed from $[\mathbf{1}\text{-}Fe^VO]^{1-}$ and $[\mathbf{1}\text{-}Fe^{IV}O]^{2-}$, respectively, were both absent, which indicates a change in the axial ligand for the green species. For an $Fe^{IV}OH_n$ ($n = 1$ or 2) species, the elongated $Fe{-}OH_n$ bond when compared with Fe-oxo bond may result in dramatic red shift of the $Fe{-}OH_n$ stretching vibration to a spectral region where spectral features are dominated by other metal−ligand vibrational bands (<600 cm^{-1}).

DFT Calculations of $[\mathbf{1}\text{-}Fe^VO]^-$. DFT calculations of the several high-valent Fe-TAML adducts were performed with the aim of identifying the structure of the low-pH green species on the basis of its hyperfine parameters, zero-field splitting, and vibrational frequencies. DFT calculations of $[\mathbf{1}\text{-}Fe^VO]^-$ generated Mössbauer parameters in close agreement with experiment (Table 1). The parameters did not vary significantly from those for $[\mathbf{2}\text{-}Fe^VO]^-$ and $[\mathbf{3}\text{-}Fe^VO]^-$.[8,27] Simulations of the NRVS-derived ^{57}Fe PVDOS spectra (Figure 5) were generated from DFT frequency calculations as described in the Methods. The DFT value of ν(Fe−O) for $[\mathbf{1}\text{-}Fe^VO]^-$ of 909 cm^{-1} (Figure 5A, dashed line) was higher than the experimental value of 876 cm^{-1}. DFT-calculated ν(Fe−O) energies often are higher than experiment and have been empirically corrected by a multiplication factor smaller than 1, of which the value depends on the functional/basis set combination used. However, without an empirical correction, the DFT simulated NRVS spectrum is in approximate agreement with the lower energy bands (400−500 cm^{-1}) that are principally Fe−N vibrations. Changing the frequency scale by an empirical factor that would align the ν(Fe−O) energy with experiment would then shift the Fe−N bands out of agreement. Instead, we expect in aqueous solution that water is likely forming hydrogen bonds to the oxo of the FeO unit. A molecule of water at hydrogen bond distance was added, and the optimized structure showed retention of the hydrogen bond to the water. The DFT-simulated NRVS spectrum with the addition water (Figure 5A, solid line) showed a 25 cm^{-1} downward shift in the ν(Fe−O) energy to 884 nm^{-1}, bringing the band close to experiment but without causing changes in either the Fe−N bands or hyperfine parameters (cf. Table S1). As shown below, the addition of water with hydrogen bonds to the iron−oxo unit were found to have a similar effect for the other complexes.

The ν(Fe−O) vibration of $[\mathbf{1}\text{-}Fe^VO]^{1-}$ at 876 cm^{-1} is higher than that of $[\mathbf{3}\text{-}Fe^VO]^{1-}$ at 862 cm^{-1}.[29] The DFT value of ν(Fe−O) for both complexes is approximately equal, suggesting that the increased basicity of the **1** macrocycle is not the cause of the different experimental values of ν(Fe−O). Similar to $[\mathbf{1}\text{-}Fe^VO]^{1-}$, the low value for $[\mathbf{3}\text{-}Fe^VO]^{1-}$ relative to the DFT value suggests that hydrogen bonds possibly from water may also be present in $[\mathbf{3}\text{-}Fe^VO]^{1-}$.

DFT Calculations of $[\mathbf{1}\text{-}Fe^{IV}O]^{2-}$. DFT calculations of the $[\mathbf{1}\text{-}Fe^{IV}O]^{2-}$ complex gave Mössbauer parameters, including isomer shift, quadrupole splitting, and magnetic hyperfine parameters, that were in good agreement with experiment (Table 1). DFT calculations were also performed on $[\mathbf{2}\text{-}Fe^{IV}O]^{2-}$ and $\mathbf{2}\text{-}Fe^{IV}_2(\mu\text{-oxo})$ and gave a similarly good agreement (Table S1). In addition, these calculations show that the electronic properties of the $Fe^{IV}O$ complexes are similar across different TAML variants. The NRVS-derived ^{57}Fe PVDOS spectrum of $[\mathbf{1}\text{-}Fe^{IV}O]^{2-}$ showed a ν(Fe−O) vibration at 764 cm^{-1}. This value was considerably lower than the ν(Fe−O) energies in other $Fe^{IV}O$ complexes, with $[\mathbf{3}\text{-}Fe^{IV}O]^{2-}$ having the next lowest ν(Fe−O) at 798 cm^{-1}.[29] The increased basicity of the **1** macrocyle is expected to the lower ν(Fe−O) energy, as was suggested for **3** previously.[30] DFT calculations gave ν(Fe−O) energies at 825 cm^{-1} for $[\mathbf{1}\text{-}Fe^{IV}O]^{2-}$ (Figure 5B, dashed line). As with $[\mathbf{1}\text{-}Fe^VO]^-$, the DFT-calculated ν(Fe−O) energy was significantly higher than experiment. In aqueous solution, $[\mathbf{1}\text{-}Fe^{IV}O]^{2-}$ may form a hydrogen bond between the iron−oxo unit and water. Inclusion of hydrogen bonds of $Fe^{IV}O$ compounds has been shown to assist in more accurate modeling of electronic parameters by DFT for $[\mathbf{2}\text{-}Fe^{IV}O]^{2-}$.[26] Indeed, when two water molecules were added to form a hydrogen bonds with the oxo in $[\mathbf{1}\text{-}Fe^{IV}O]^{2-}$, the DFT-calculated ν(Fe−O) energy dropped to 763 cm^{-1}, in close agreement with experiment (Figure 5B, solid line). As in the case of the $[\mathbf{1}\text{-}Fe^VO]^-$, the changes in the hyperfine parameters caused by the hydrogen bonds are minor (Table S1).

DFT Calculations of the Green Fe^{IV} Species. The change in spin state and lack of an observable ν(Fe−O) band in the low-pH green Fe^{IV} species implied a significant coordination change from $Fe^{IV}O$ at high pH. Two types of structural changes were considered that could change the Fe−O interaction in $Fe^{IV}O$. The generation of the green Fe^{IV}

DOI: 10.1021/acs.inorgchem.8b03200
Inorg. Chem. XXXX, XXX, XXX−XXX

species at low pH implied protonation of either the iron−oxo unit or the macrocycle.

Previously, a protonated complex of $[Fe^{IV}H_3buea(O)]^-$ (H_3buea = tris[(*N′-tert*-butylureaylato)-*N*-ethylene]aminato) was suspected to have been $Fe^{IV}OH$, but careful analysis indicated instead that the ligand was protonated.[5] To rule out ligand protonation in this situation, rather than FeO protonation, DFT optimization of $[\mathbf{1}\text{-}Fe^{IV}O]^{2-}$ protonated on one of the amido nitrogens in the **1** macrocycle was performed to mimic a partial reversal of the deprotonation required in the metalation process. The calculation indicated that ligand-protonated $[\mathbf{1}\text{-}Fe^{IV}O]^{2-}$ retained a ν(Fe−O) band at 763 cm^{-1} which is absent in the NRVS data for the green species and that the hyperfine parameters differ significantly from those of the green species (cf. Table S1). Similarly, NRVS spectra of $[Fe^{IV}H_3buea(O)]^-$ showed the ν(Fe−O) frequency did not change upon protonation, which was critical evidence to support ligand rather than oxo protonation.[5] Accordingly, the loss of the ν(Fe−O) vibration at 763 cm^{-1} in the green Fe^{IV} species implicates a change from oxo coordination.

Protonation of the iron−oxo unit could suggest either $Fe^{IV}OH$ or $Fe^{IV}OH_2$ formation. DFT optimizations of $[\mathbf{1}\text{-}Fe^{IV}OH]^-$ and $[\mathbf{1}\text{-}Fe^{IV}OH_2]^0$ were next performed. ORCA calculations of the axial zero-field parameter D showed that its sign was negative and in approximate agreement with experimental data. The Mössbauer parameters from DFT are in good agreement with experimental data (Table 1). Protonation of the iron−oxo unit to give $[\mathbf{1}\text{-}Fe^{IV}OH]^-$ was calculated to lengthen the Fe−O bond from 1.67 to 1.94 Å. The longer Fe−O bond length coincided with a marked drop in the ν(Fe−O) energy to 475 cm^{-1} (Figure 5C, dashed line). When a hydrogen bond to a water molecule was included, the ν(Fe−O) energy further dropped and the band split into two features at 463 and 447 cm^{-1} (Figure 5C, solid line). The protonation induced lengthening of the Fe−O bond leads to a decrease in the energy of the d_{z^2} orbital to permit a high-spin configuration, $(d_{xy})(d_{xz})(d_{yz})(d_{z^2})$; such an electronic state change would also elicit the large changes to δ and ΔE_Q observed experimentally and reproduced with DFT. The latter configuration differs from the low-lying excited S = 2 $(d_{xy})(d_{xz})(d_{yz})(d_{x^2-y^2})$ configuration that gives rise to the large zero-field splitting in S = 1 Fe^{IV}-oxo species (Table 1) by spin−orbit interaction with the S = 1 $(d_{xy^2})(d_{xz})(d_{yz})$ ground state.[33] The change of ground state in $[\mathbf{1}\text{-}FeOH]^-$ disables the mechanism that gives rise to the large D value in S = 1 Fe^{IV}-oxo species and replaces it with a new set of spin−orbit interactions that yield a small negative D value (see Table 1). The calculations for $[\mathbf{1}\text{-}Fe^{IV}OH_2]^0$ gave similar results. Similar DFT experiments have been performed to demonstrate the protonation of $Fe^{IV}O$ in ferryl heme species.[34]

DISCUSSION

The influence of structural variations of TAMLs on the properties of its iron complexes have been extensively characterized by spectroscopic methods. These investigations have built a catalog of spectroscopic parameters for the different macrocycle variants. The catalog shows that despite changes to the core macrocycle, the fine structure, and hyperfine parameters of the TAML variants are largely conserved for equivalent oxidation states. These relations provide a basis for comparison for the high-valent species found for **1**. In the context of the present discussion, the comparison to past data has allowed characterization of the high-valent species generated from oxidation of **1**, thereby highlighting the novelty of the low pH green complex.

Electrochemical experiments demonstrated that the low pH species was one oxidation equivalent above Fe^{III}. The formation of the same green species by both bulk electrolysis and oxidation by cerium demonstrated that the structure of the species was not a function of the oxidation process. One possibility is an Fe^{III}-ligand radical species. A recent paper proposed the isolation of a corrole-based $Fe^{IV}O$ complex, with the caveat that one electron oxidized Fe^{III} corroles often form Fe^{III}-ligand radical species, as opposed to true Fe^{IV} complexes. Indeed, the Mössbauer isomer shifts of the proposed Fe^{IV} corroles are suggestive of ligand oxidation, rather than Fe oxidation.[6] Fortunately, in the case of TAMLs, a Fe^{III}-ligand radical TAML complex has been spectroscopically characterized and is distinct from the new green species.[10] The spin state, isomer shift, quadrupole splitting, and magnetic hyperfine parameters of the green species generated from **1** unequivocally assign the oxidation state as Fe^{IV}.

We dismiss the possibility that Fe^{IV} was not in bound to TAML since the Fe^{III} species of the same ligand were stable at pH 2, the electrochemistry was reversible and Mössbauer parameters of Fe^{IV} in water were much different.[35] Fe^{IV} TAML complexes can form dimers,[9] but the addition of out-of-plane methyl functional groups of **1** provide steric hindrance to disfavor dimerization. The spectroscopic data did not show formation of dimeric species at any pH or oxidation state. We have considered the formation of a dimeric species in which two equal S = 1 Fe^{IV} sites are bridged by hydroxo. An S = 2 state could result from a ferromagnetic exchange interaction through the hydroxo bridge. However, we can rule out such a dimer complex since the isotropic value of the A-tensor of the green species (A_{iso} = −14 T) is close to that of the monomeric S = 2 $[\mathbf{4}\text{-}Fe^{IV}Cl]^-$ complex (A_{iso} = −15 T).[31] If the green Fe^{IV} complex were dimeric, then the value of A_{iso} for an S = 1 Fe^{IV} site would be −28 T (A_{couple} = 1/2 A_{site}), which is much higher than for any other S = 1 Fe^{IV} TAML complex (A_{iso} ∼ 20 T) and in general too high for iron.

The combined electrochemical and spectroscopic data indicate that the green species prepared from **1** has properties markedly different than all known iron−oxo TAML variants. The generation of the green Fe^{IV} species at low pH indicates the green species as a protonated Fe^{IV} complex. DFT calculations have shown that protonation on the macrocycle was incompatible with the experimental spectroscopic data. However, protonation of $Fe^{IV}O$ satisfied all experimental constraints. DFT calculations for the S = 2 states of both $[\mathbf{1}\text{-}Fe^{IV}OH]^-$ and $[\mathbf{1}\text{-}Fe^{IV}OH_2]^0$ gave zero-field splitting, isomer shift, quadrupole splitting, and hyperfine tensor which are compatible with experiment. The S = 2 state for the green species, in contrast to all other $Fe^{IV}O$ TAMLs which are S = 1, primarily results from disruption of the strong iron−oxo interaction, causing a lengthening of the Fe−O bond, which lowers the energy of the d_{z^2} orbital. The resulting spin state reconfiguration is responsible for the change in isomer shift, quadrupole splitting, and zero-field splitting relative to the S = 1 $Fe^{IV}O$ complexes, which have been described previously.[26] Consistent with the longer Fe−O bond, the protonation of $Fe^{IV}O$ significantly lowers the Fe−O vibration frequency.[36] The NRVS of the green Fe^{IV} species showed loss of the Fe^{IV}−O vibration at 763 cm^{-1} present at high pH. DFT calculations of NRVS spectra were shown to give accurate Fe−O vibrational frequencies of all characterized Fe^{IV} and Fe^{V}

DOI: 10.1021/acs.inorgchem.8b03200
Inorg. Chem. XXXX, XXX, XXX−XXX

TAML variants and predicted a Fe−O frequency at 475 cm^{-1} for $[\mathbf{1}\text{-}Fe^{IV}OH]^-$. The predicted Fe−O vibration energy overlaps with the $Fe-N_{amido}$ vibrations and is split by hydrogen bonding, preventing clear confirmation of the peak assignment. The combined spectroscopic data and DFT calculations indicate that the low pH green species is either $[\mathbf{1}\text{-}Fe^{IV}OH]^-$ or $[\mathbf{1}\text{-}Fe^{IV}OH_2]^0$. The electrochemical data between pH 2 and 3 indicates that the protonation state of the complex does not change for the $Fe^{III/IV}$ transition. At pH 2, the Fe^{3+} complex has an axial H_2O;[7] therefore, upon oxidation the green species is either $[\mathbf{1}\text{-}Fe^{IV}OH_2]^0$ or $[\mathbf{1}\text{-}Fe^{IV}OH^- + H^+]^0$ in which a proton has transferred from the axial water to the macrocyclic ligand. Alternatively, the proton transfer may not be electron coupled and the oxidized complex of the spectroscopic samples is $[\mathbf{1}\text{-}Fe^{IV}OH]^-$.

$Fe^{IV}O$ in Context of H Atom Abstraction. $Fe^{IV}O$ has been implicated in the key reactive step in hydroxylation of C−H bonds by P450 Type enzymes. These enzymes employ a heme iron to activate oxygen to generate a two-electron oxidized Compound I species (Cpd-I), which is an $Fe^{IV}O$-porphyrin radical species. Cpd-I then abstracts an H atom from the substrate to generate Cpd-II ($Fe^{IV}OH$) and carbon radical on the substrate. This species is highly reactive, and rapidly the iron-bound hydroxide rebounds to the carbon radical to generate the hydroxylated product and Fe^{III} porphyrin. The stabilization of a protonated Cpd-II, and preference toward productive oxidation of substrate (rather than harmful oxidation of the protein) has been correlated to the pK_a of the iron oxo unit. In thiolate-ligated P450 enzymes, the pK_a of the $Fe^{IV}O$ is 11.9.[4] In Myoglobin-type enzymes, where oxidation chemistry is not desired, the measured pK_a of the $Fe^{IV}O$ is approximately 2.[37] The low pK_a's of myoglobin and horseradish peroxidase prohibit generation of $Fe^{IV}OH$ under physiological conditions and thus prevents undesired hydroxylation via a protonated Cpd-II.

Protonation of the iron−oxo unit has proved to be remarkably difficult for synthetic complexes. To date, attempts to make synthetic analogs have been unsuccessful. The chemistry of TAML compounds has been shown to have similarities to that of P450. The Fe^{III} TAML is activated to the $Fe^{V}O$ state (formally equivalent to the oxidation state of Cpd-I), which abstracts an H atom from the substrate.[38] An $Fe^{IV}OH$ and substrate radical have been proposed to be the transient state following H atom abstraction, but to date, this intermediate has not been trapped. Interestingly, $OH^{\bullet}$ rebound has been suggested in reactions of **3** with alkanes to be an unproductive pathway: $OH^{\bullet}$ rebound from the purported $Fe^{IV}OH$ to generate the oxidized product and the reduced $Fe^{III}OH_2$ complex, which undergoes rapid comproportionation with $Fe^{V}O$ to from the catalytically inert μ-oxo-Fe^{IV}_2 product.[27] Kinetic studies showed that the comproportionation reaction rate was 10^5-fold faster than the rate for C−H bond activation. Rapid generation of the μ-oxo-Fe^{IV}_2 product effectively stopped all further reaction and limited the yield of oxidized product to 50%.

While past TAML complexes had been inactivated via dimerization following $OH^{\bullet}$ rebound, the steric effects of the aliphatic **1** macrocycle prevent dimer formation. As discussed above, dimer formation was rapid following H atom abstraction with **3**. In the case of **1**, the inability to form stable dimers perhaps increases the stabilization of the $Fe^{IV}OH$ species during turnover and possibly allows $OH^{\bullet}$ rebound as the major substrate oxidation pathway. Furthermore, the stability of the high-valent oxidation states of **1** in pure water is unique among all TAML variants. Previously, **3** was shown to stabilize $Fe^{V}O$ in up to 70% water and shows better reactivity of toluene oxidation as the amount of water was increased (60-fold increase in toluene oxidation in 70:30 H_2O/CH_3CN vs pure CH_3CN).[39] The authors suggested that the H-bonding interactions with the water solvent played a role in stabilization of the transient $Fe^{IV}O$ species and lowering of the Fe−O bond dissociation energy, thereby increasing the rate of reaction. Thus, the unique stability of **1** complexes in water could contribute to the stability of the $Fe^{IV}OH$ species and possibly the design of synthetic complexes stable in aqueous environments could bolster the development of subsequent synthetic $Fe^{IV}OH$ complexes.

The $[\mathbf{1}\text{-}Fe^{IV}OH]^-$ or $[\mathbf{1}\text{-}Fe^{IV}OH_2]^0$ complex was stable below pH 2, whereas at higher pH the complex decayed to Fe^{III} species with ligand degradation. Its instability above pH 2 and the instability of $[\mathbf{1}\text{-}Fe^{IV}O]^{2-}$ below pH 10 would suggest a pK_a in the range of 2−10. It is difficult to place this pK_a in the context of other TAML variants, given that all other TAMLs can only generate high-valent species in organic solvents or under very basic conditions. In the context of heme enzymes capable of supporting a protonated Cpd-II, the pK_a of $Fe^{IV}O$ **1** is low. For P450, the Cpd-II species has pK_a of 11.9, which is a function of the increased basicity induced by the axial thiolate.[4] In contrast, histidine ligated hemes, such as Mb and HRP, have pK_a values of $\leq$2.7 and $\leq$3.6, respectively, and cannot easily support a protonated Cpd-II.[37] The **1** macrocycle, with no thiol coordination ligands but with greater electron donation from the macrocycle, has a pK_a closer to that of HRP and Mb. Fortunately, in the case of **1**, the pK_a is sufficiently high to allow isolation of a novel $Fe^{IV}O$ complex.

CONCLUSION

The first axially protonated synthetic $Fe^{IV}O$ complex has been generated and spectroscopically characterized. At pH 2, the stable complex is either $[\mathbf{1}\text{-}Fe^{IV}OH]^-$ or $[\mathbf{1}\text{-}Fe^{IV}OH_2]^0$. DFT calculations demonstrate that the spectroscopic parameters of the green complex are compatible with either configuration. While previous TAML variants are believed to transiently form $Fe^{IV}OH$ species, the $Fe^{IV}OH$ species presumably rapidly dimerizes to other complexes, making detection difficult. The steric bulk provided by the replacement of the aryl group with the $-CMe_2CMe_2-$ unit in **1** prevents dimerization in all oxidation states over a wide pH range, thus allowing the generation of either $[\mathbf{1}\text{-}Fe^{IV}OH]^-$ or $[\mathbf{1}\text{-}Fe^{IV}OH_2]^0$ in near quantitative yield from oxidation of **1**.

ASSOCIATED CONTENT

Supporting Information

The Supporting Information is available free of charge on the ACS Publications website at DOI: 10.1021/acs.inorgchem.8b03200.

Electrochemical data, electronic absorption spectrum with cerium, EPR spectrum of $[\mathbf{1}\text{-}Fe^{IV}Cl]^-$, electronic and nuclear parameters of selected TAML complexes from DFT calculations, reference to Gaussian 09. (PDF)

AUTHOR INFORMATION

Corresponding Authors

*E-mail: hendrich@andrew.cmu.edu (M.P.H.).
*E-mail: eb7g@andrew.cmu.edu (E.L.B.).

DOI: 10.1021/acs.inorgchem.8b03200
Inorg. Chem. XXXX, XXX, XXX−XXX

ORCID

Matthew R. Mills: 0000-0001-8975-2855
Alexander D. Ryabov: 0000-0002-5255-1395
Terrence J. Collins: 0000-0003-2611-9184
Yisong Guo: 0000-0002-4132-3565
Emile L. Bominaar: 0000-0002-5125-265X
Michael P. Hendrich: 0000-0003-4775-0389

Notes

The authors declare no competing financial interest.

■ ACKNOWLEDGMENTS

The work was funded by NIH R01 GM077387 (M.P.H.) and NSF CHE1654060 (Y.G.). T.J.C. thanks the Heinz Endowments for support. Funding for the EPR spectrometer was from NSF CHE1126268.

■ REFERENCES

(1) Ortiz de Montellano, P. R. Hydrocarbon Hydroxylation by Cytochrome P450 Enzymes. *Chem. Rev.* **2010**, *110*, 932−948.

(2) Casadei, C. M.; Gumiero, A.; Metcalfe, C. L.; Murphy, E. J.; Basran, J.; Concilio, M. G.; Teixeira, S. C.; Schrader, T. E.; Fielding, A. J.; Ostermann, A.; Blakeley, M. P.; Raven, E. L.; Moody, P. C. Heme Enzymes. Neutron Cryo-Crystallography Captures the Protonation State of Ferryl Heme in a Peroxidase. *Science* **2014**, *345*, 193−197.

(3) Chreifi, G.; Baxter, E. L.; Doukov, T.; Cohen, A. E.; McPhillips, S. E.; Song, J.; Meharenna, Y. T.; Soltis, S. M.; Poulos, T. L. Crystal Structure of the Pristine Peroxidase Ferryl Center and Its Relevance to Proton-Coupled Electron Transfer. *Proc. Natl. Acad. Sci. U. S. A.* **2016**, *113*, 1226−1231.

(4) Yosca, T. H.; Rittle, J.; Krest, C. M.; Onderko, E. L.; Silakov, A.; Calixto, J. C.; Behan, R. K.; Green, M. T. Iron(Iv)Hydroxide Pk(a) and the Role of Thiolate Ligation in C-H Bond Activation by Cytochrome P450. *Science* **2013**, *342*, 825−829.

(5) Hill, E. A.; Weitz, A. C.; Onderko, E.; Romero-Rivera, A.; Guo, Y.; Swart, M.; Bominaar, E. L.; Green, M. T.; Hendrich, M. P.; Lacy, D. C.; Borovik, A. S. Reactivity of an Feiv-Oxo Complex with Protons and Oxidants. *J. Am. Chem. Soc.* **2016**, *138*, 13143−13146.

(6) Zaragoza, J. P. T.; Yosca, T. H.; Siegler, M. A.; Moenne-Loccoz, P.; Green, M. T.; Goldberg, D. P. Direct Observation of Oxygen Rebound with an Iron-Hydroxide Complex. *J. Am. Chem. Soc.* **2017**, *139*, 13640−13643.

(7) Mills, M. R.; Weitz, A. C.; Zhang, D. Z.; Hendrich, M. P.; Ryabov, A. D.; Collins, T. J. A "Beheaded" Taml Activator: A Compromised Catalyst That Emphasizes the Linearity between Catalytic Activity and Pka. *Inorg. Chem.* **2016**, *55*, 12263−12269.

(8) Mills, M. R.; Weitz, A. C.; Hendrich, M. P.; Ryabov, A. D.; Collins, T. J. Naclo-Generated Iron(Iv)Oxo and Iron(V)Oxo Tamls in Pure Water. *J. Am. Chem. Soc.* **2016**, *138*, 13866−13869.

(9) Chanda, A.; de Oliveira, F. T.; Collins, T. J.; Munck, E.; Bominaar, E. L. Density Functional Theory Study of the Structural, Electronic, and Magnetic Properties of a Mu-Oxo Bridged Dinuclear Fe(Iv) Complex Based on a Tetra-Amido Macrocyclic Ligand. *Inorg. Chem.* **2008**, *47*, 9372−9379.

(10) Bartos, M. J.; Kidwell, C.; Kauffmann, K. E.; Gordon-Wylie, S. W.; Collins, T. J.; Clark, G. C.; Münck, E.; Weintraub, S. T. A Stable Aquairon(Iii) Complex with S = 1: Structure and Spectroscopic Properties. *Angew. Chem., Int. Ed. Engl.* **1995**, *34*, 1216−1219.

(11) Kojima, T.; Ogishima, F.; Nishibu, T.; Kotani, H.; Ishizuka, T.; Okajima, T.; Nozawa, S.; Shiota, Y.; Yoshizawa, K.; Ohtsu, H.; Kawano, M.; Shiga, T.; Oshio, H. Intermediate-Spin Iron(Iii) Complexes Having a Redox-Noninnocent Macrocyclic Tetraamido Ligand. *Inorg. Chem.* **2018**, *57*, 9683−9695.

(12) DeNardo, M. A.; Mills, M. R.; Ryabov, A. D.; Collins, T. J. Unifying Evaluation of the Technical Performances of Iron-Tetra-Amido Macrocyclic Ligand Oxidation Catalysts. *J. Am. Chem. Soc.* **2016**, *138*, 2933−2936.

(13) Petasis, D. T.; Hendrich, M. P. Quantitative Interpretation of Multifrequency Multimode Epr Spectra of Metal Containing Proteins, Enzymes, and Biomimetic Complexes. *Methods Enzymol.* **2015**, *563*, 171−208.

(14) Abragam, A.; Bleaney, B. *Electron Paramagnetic Resonance of Transition Ions*; Clarendon Press: Oxford, 1970.

(15) Sturhahn, W. Nuclear Resonant Spectroscopy. *J. Phys.: Condens. Matter* **2004**, *16*, S497−S530.

(16) Toellner, T. S. Monochromatization of Synchrotron Radiation for Nuclear Resonant Scattering Experiments. *Hyperfine Interact.* **2000**, *125*, 3−28.

(17) Sturhahn, W. Conuss and Phoenix: Evaluation of Nuclear Resonant Scattering Data. *Hyperfine Interact.* **2000**, *125*, 149−172.

(18) Frisch, M. J.; Trucks, G. W.; Schlegel, H. B.; Scuseria, G. E.; Robb, M. A.; Cheeseman, J. R.; Scalmani, G.; Barone, V.; Mennucci, B.; Petersson, G. A.; Nakatsuji, H.; Caricato, M.; Li, X.; Hratchian, H. P.; Izmaylov, A. F.; Bloino, J.; Zheng, G.; Sonnenberg, J. L.; Hada, M.; Ehara, M.; Toyota, K.; Fukuda, R.; Hasegawa, J.; Ishida, M.; Nakajima, T.; Honda, Y.; Kitao, O.; Nakai, H.; Vreven, T.; Montgomery, J. A., Jr.; Peralta, J. E.; Ogliaro, F.; Bearpark, M.; Heyd, J. J.; Brothers, E.; Kudin, K. N.; Staroverov, V. N.; Kobayashi, R.; Normand, J.; Raghavachari, K.; Rendell, A.; Burant, J. C.; Iyengar, S. S.; Tomasi, J.; Cossi, M.; Rega, N.; Millam, J. M.; Klene, M.; Knox, J. E.; Cross, J. B.; Bakken, V.; Adamo, C.; Jaramillo, J.; Gomperts, R.; Stratmann, R. E.; Yazyev, O.; Austin, A. J.; Cammi, R.; Pomelli, C.; Ochterski, J. W.; Martin, R. L.; Morokuma, K.; Zakrzewski, V. G.; Voth, G. A.; Salvador, P.; Dannenberg, J. J.; Dapprich, S.; Daniels, A. D.; Farkas, O.; Foresman, J. B.; Ortiz, J. V.; Cioslowski, J.; Fox, D. J. *Gaussian 09*, revision D.01; Gaussian, Inc.: Wallingford, CT, 2009.

(19) Vrajmasu, V.; Munck, E.; Bominaar, E. L. Density Functional Study of the Electric Hyperfine Interactions and the Redox-Structural Correlations in the Cofactor of Nitrogenase. Analysis of General Trends in (57)Fe Isomer Shifts. *Inorg. Chem.* **2003**, *42*, 5974−5988.

(20) Neese, F. The Orca Program System. *Wires Comput. Mol. Sci.* **2012**, *2*, 73−78.

(21) Weigend, F.; Ahlrichs, R. Balanced Basis Sets of Split Valence, Triple Zeta Valence and Quadruple Zeta Valence Quality for H to Rn: Design and Assessment of Accuracy. *Phys. Chem. Chem. Phys.* **2005**, *7*, 3297−3305.

(22) Schafer, A.; Horn, H.; Ahlrichs, R. Fully Optimized Contracted Gaussian-Basis Sets for Atoms Li to Kr. *J. Chem. Phys.* **1992**, *97*, 2571−2577.

(23) Sage, J. T.; Paxson, C.; Wyllie, G. R. A.; Sturhahn, W.; Durbin, S. M.; Champion, P. M.; Alp, E. E.; Scheidt, W. R. Nuclear Resonance Vibrational Spectroscopy of a Protein Active-Site Mimic. *J. Phys.: Condens. Matter* **2001**, *13*, 7707−7722.

(24) Mills, M. R.; Shen, L. Q.; Zhang, D. Z.; Ryabov, A. D.; Collins, T. J. Iron(Iii) Ejection from a "Beheaded" Taml Activator: Catalytically Relevant Mechanistic Insight into the Deceleration of Electrophilic Processes by Electron Donors. *Inorg. Chem.* **2017**, *56*, 10226−10234.

(25) Popescu, D.-L.; Vrabel, M.; Brausam, A.; Madsen, P.; Lente, G.; Fabian, I.; Ryabov, A. D.; van Eldik, R.; Collins, T. J. Thermodynamic, Electrochemical, High-Pressure Kinetic, and Mechanistic Studies of the Formation of Oxo Feiv-Taml Species in Water. *Inorg. Chem.* **2010**, *49*, 11439−11448.

(26) Chanda, A.; Shan, X.; Chakrabarti, M.; Ellis, W. C.; Popescu, D. L.; Tiago de Oliveira, F.; Wang, D.; Que, L., Jr.; Collins, T. J.; Munck, E.; Bominaar, E. L. (Taml)Feiv O Complex in Aqueous Solution: Synthesis and Spectroscopic and Computational Characterization. *Inorg. Chem.* **2008**, *47*, 3669−3678.

(27) Ghosh, M.; Singh, K. K.; Panda, C.; Weitz, A.; Hendrich, M. P.; Collins, T. J.; Dhar, B. B.; Sen Gupta, S. Formation of a Room Temperature Stable Fe(V)(O) Complex: Reactivity toward Unactivated C-H Bonds. *J. Am. Chem. Soc.* **2014**, *136*, 9524−9527.

(28) de Oliveira, F. T.; Chanda, A.; Banerjee, D.; Shan, X.; Mondal, S.; Que, L., Jr.; Bominaar, E. L.; Munck, E.; Collins, T. J. Chemical

DOI: 10.1021/acs.inorgchem.8b03200
Inorg. Chem. XXXX, XXX, XXX−XXX

and Spectroscopic Evidence for an Fev-Oxo Complex. *Science* **2007**, *315*, 835−838.
(29) McDonald, A. R.; Que, L., Jr High-Valent Nonheme Iron-Oxo Complexes: Synthesis, Structure, and Spectroscopy. *Coord. Chem. Rev.* **2013**, *257*, 414−428.
(30) Pattanayak, S.; Jasniewski, A. J.; Rana, A.; Draksharapu, A.; Singh, K. K.; Weitz, A.; Hendrich, M.; Que, L.; Dey, A.; Sen Gupta, S. Spectroscopic and Reactivity Comparisons of a Pair of Btaml Complexes with Fev═O and Feiv═O Units. *Inorg. Chem.* **2017**, *56*, 6352−6361.
(31) Kostka, K. L.; Fox, B. G.; Hendrich, M. P.; Collins, T. J.; Rickard, C. E. F.; Wright, L. J.; Munck, E. High-Valent Transition Metal Chemistry. Mössbauer and Epr Studies of High-Spin (S = 2) Iron(Iv) and Intermediate-Spin (S = 3/2) Iron(Iii) Complexes with a Macrocyclic Tetraamido-N Ligand. *J. Am. Chem. Soc.* **1993**, *115*, 6746−6757.
(32) Ghosh, A.; Ryabov, A. D.; Mayer, S. M.; Horner, D. C.; Prasuhn, D. E., Jr.; Sen Gupta, S.; Vuocolo, L.; Culver, C.; Hendrich, M. P.; Rickard, C. E. F.; Norman, R. E.; Horwitz, C. P.; Collins, T. J. Understanding the Mechanism of H+-Induced Demetalation as a Design Strategy for Robust Iron(Iii) Peroxide-Activating Catalysts. *J. Am. Chem. Soc.* **2003**, *125*, 12378−12379.
(33) Sinnecker, S.; Svensen, N.; Barr, E. W.; Ye, S.; Bollinger, J. M., Jr.; Neese, F.; Krebs, C. Spectroscopic and Computational Evaluation of the Structure of the High-Spin Fe(Iv)-Oxo Intermediates in Taurine: Alpha-Ketoglutarate Dioxygenase from Escherichia Coli and Its His99ala Ligand Variant. *J. Am. Chem. Soc.* **2007**, *129*, 6168−6179.
(34) Stone, K. L.; Hoffart, L. M.; Behan, R. K.; Krebs, C.; Green, M. T. Evidence for Two Ferryl Species in Chloroperoxidase Compound Ii. *J. Am. Chem. Soc.* **2006**, *128*, 6147−6153.
(35) Pestovsky, O.; Stoian, S.; Bominaar, E. L.; Shan, X.; Munck, E.; Que, L., Jr.; Bakac, A. Aqueous Feiv═O: Spectroscopic Identification and Oxo-Group Exchange. *Angew. Chem., Int. Ed.* **2005**, *44*, 6871−6874.
(36) Green, M. T. Application of Badger's Rule to Heme and Non-Heme Iron-Oxygen Bonds: An Examination of Ferryl Protonation States. *J. Am. Chem. Soc.* **2006**, *128*, 1902−1906.
(37) Yosca, T. H.; Behan, R. K.; Krest, C. M.; Onderko, E. L.; Langston, M. C.; Green, M. T. Setting an Upper Limit on the Myoglobin Iron(Iv)Hydroxide Pk(a): Insight into Axial Ligand Tuning in Heme Protein Catalysis. *J. Am. Chem. Soc.* **2014**, *136*, 9124−9131.
(38) Collins, T. J.; Ryabov, A. D. Targeting of High-Valent Iron-Taml Activators at Hydrocarbons and Beyond. *Chem. Rev.* **2017**, *117*, 9140−9162.
(39) Singh, K. K.; Tiwari, M.; Ghosh, M.; Panda, C.; Weitz, A.; Hendrich, M. P.; Dhar, B. B.; Vanka, K.; Sen Gupta, S. Tuning the Reactivity of Fe(V)(O) toward C-H Bonds at Room Temperature: Effect of Water. *Inorg. Chem.* **2015**, *54*, 1535−1542.

DOI: 10.1021/acs.inorgchem.8b03200
Inorg. Chem. XXXX, XXX, XXX−XXX